

**Electrostatic engineering of strained ferroelectric perovskites from first principles**

Claudio Cazorla

*School of Materials Science and Engineering, UNSW Australia, Sydney, NSW 2052, Australia  
and Integrated Materials Design Centre, UNSW Australia, Sydney, NSW 2052, Australia*

Massimiliano Stengel

*Institut de Ciència de Materials de Barcelona (ICMAB-CSIC), 08193 Bellaterra, Spain  
and ICREA—Institució Catalana de Recerca i Estudis Avançats, 08010 Barcelona, Spain*

(Received 6 October 2015; published 14 December 2015)

Design of novel artificial materials based on ferroelectric perovskites relies on the basic principles of electrostatic coupling and in-plane lattice matching. These rules state that the out-of-plane component of the electric displacement field and the in-plane components of the strain are preserved across a layered superlattice, provided that certain growth conditions are respected. Intense research is currently directed at optimizing materials functionalities based on these guidelines, often with remarkable success. Such principles, however, are of limited practical use unless one disposes of reliable data on how a given material behaves under arbitrary electrical and mechanical boundary conditions. Here we demonstrate, by focusing on the prototypical ferroelectrics  $\text{PbTiO}_3$  and  $\text{BiFeO}_3$  as test cases, how such information can be calculated from first principles in a systematic and efficient way. In particular, we construct a series of two-dimensional maps that describe the behavior of either compound (e.g., concerning the ferroelectric polarization and antiferrodistortive instabilities) at any conceivable choice of the in-plane lattice parameter,  $a$ , and out-of-plane electric displacement,  $D$ . In addition to being of immediate practical applicability to superlattice design, our results bring new insight into the complex interplay of competing degrees of freedom in perovskite materials and reveal some notable instances where the behavior of these materials depart from what naively is expected.

DOI: [10.1103/PhysRevB.92.214108](https://doi.org/10.1103/PhysRevB.92.214108)

PACS number(s): 77.55.Nv, 61.50.Ks, 68.65.Cd, 77.80.bn

**I. INTRODUCTION**

Perovskite-structure oxides with  $\text{ABO}_3$  formula display a wide range of functional properties that are sought after for applications in energy and nanoelectronics. Such functionalities are, to a large extent, governed by a number of symmetry-lowering lattice instabilities, which naturally occur in the crystals depending on the chemical nature of the A and B cations. Ferroelectric (FE) and antiferrodistortive (AFD) modes are by far the most common distortions in  $\text{ABO}_3$  compounds. The former are typically associated with “soft” (i.e., unstable) zone-center phonons of the reference cubic phase [see Fig. 1(a)] [1,2]. Whenever they dominate, the crystal possesses a spontaneous (and switchable) electric polarization, which can be exploited for information storage and (via the piezoelectric effect) for electromechanical transduction. The latter, on the other hand, are related to zone-boundary instabilities, whereby the oxygen octahedral cages surrounding the B cation cooperatively rotate (either in antiphase or in phase) about a particular axis [see Fig. 1(a)]. While AFD modes are nonpolar, they are extraordinarily important for the physics of magnetic perovskites, where the couplings between neighboring transition-metal sites are sensitive to the B-O-B bond angle. Cases where FE polarization and AFD distortions are present and mutually coupled in the same phase are especially intriguing from a practical and a fundamental perspective. Indeed, recent research has unveiled a number of notable examples where octahedral rotations can strongly enhance, or even induce, a ferroelectric distortion in materials that would be otherwise nonpolar [3,4]. Most importantly, such unconventional forms of ferroelectricity, often referred to as “improper” [5] or “hybrid improper” [6,7], appear as a

promising route for achieving electrical control of magnetism in multiferroics and magnetoelectrics, a tantalizing goal that has remained so far elusive in spite of the numerous recent breakthroughs [8,9].

Practical ways to manipulate and design the aforementioned functionalities are currently being investigated along two main avenues. These consist in either synthesizing new perovskite materials (e.g., by playing with the A- and B-site chemistry) or in altering the behavior of existing ones via external perturbations. In the context of the latter strategy, a large part of the recent efforts have been directed at appropriately modifying the strength of the FE and AFD instabilities (and/or their mutual interplay) via the imposed mechanical [10–13] and electrostatic boundary conditions [14–16] [see Fig. 1(b) for a summary of the most common trends].

*Strain engineering*, for instance, consists in growing the material in a thin-film form, where bonding to the substrate favors coherency in the in-plane registry. Thanks to the availability of numerous substrates with a variety of lattice parameters, such a practice has become very popular in the past few years [17,18]. Polar (FE) and structural (AFD) degrees of freedom are generally sensitive to the applied strain, and this often allows for the stabilization of phases with enhanced functional properties which would be otherwise inaccessible at the bulk level [19,20]. (The regions of parameter space that lie close to phase boundaries are particularly responsive to external perturbations because of their structural “softness” [21]).

Control of electrostatics in perovskites, on the other hand, is comparatively more subtle, as it can be easily thwarted by a redistribution of the mobile charges (e.g., electron/hole carriers, ionic defects, etc.) or the formation of ferroelectric domains. Also, leakage currents often limit the magnitude

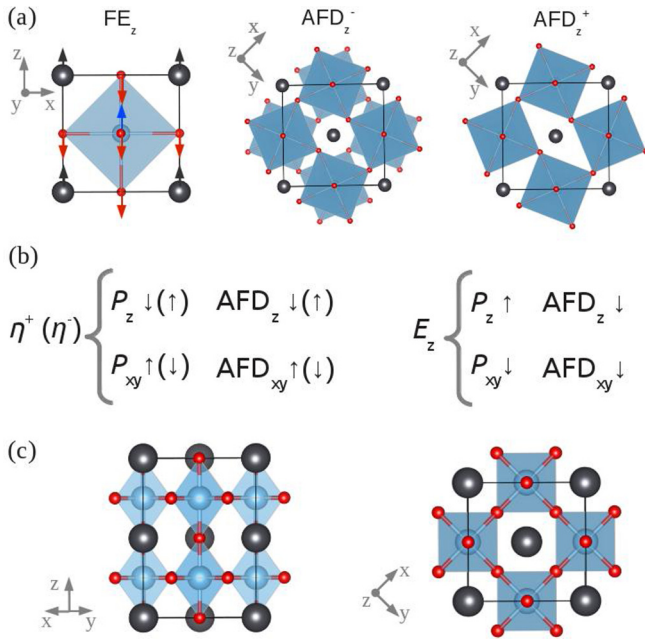


FIG. 1. (Color online) (a) Representation of typical FE and AFD distortions in perovskite oxides. (b) Expected trends of the polarization and octahedral O<sub>6</sub> rotations in oxide films upon external mechanical and electric field perturbations.  $\eta^{+(-)}$  represents a tensile (compressive) in-plane strain,  $E_z$  an out-of-plane electric field, and  $\uparrow$  ( $\downarrow$ ) an increase (decrease) in the corresponding quantity. (c) Sketch of the 20-atom  $\sqrt{2} \times \sqrt{2} \times 2$  simulation cell used in our calculations; red, blue, and black spheres represent O, B, and A atoms in  $ABO_3$  perovskites, respectively. The corresponding lattice vectors are  $\mathbf{a}_1 = (a, a, 0)$ ,  $\mathbf{a}_2 = (a, -a, 0)$ , and  $\mathbf{a}_3 = (0, 0, 2a)$ , where  $a$  is the lattice parameter of the 5-atom primitive perovskite cell.

of the electric field that can be realistically applied via an external voltage source [22]. Yet the so-called *electrostatic coupling* [22–27] is one of the most valuable design principles in ferroelectric superlattices based on perovskites. It states that, at the boundary between two insulating layers, the normal component of the electric displacement field must be preserved; this effectively constrains the out-of-plane polarization state of the stack to a common value that, depending on the materials choice and conditions, might markedly differ from the spontaneous polarization of the parent compounds. In the vast majority of cases, electrostatics and strain work together and need to be simultaneously taken into account when interpreting the experiments with quantitatively predictive models.

First-principles simulations within the framework of density-functional theory (DFT) have been of invaluable help in rationalizing and guiding the experimental efforts towards synthesis of new materials with enhanced properties. Until a few years ago DFT methods were restricted to zero-electric-field simulations, which complicated the description of electrostatics in multicomponent oxide systems. Such effects have traditionally been described by means of phenomenological models, where the DFT input was limited to the computation of the relevant coupling coefficients. Recent and timely advances in first-principles computational methods have now enabled full control over the macroscopic

electrical variable of interest (i.e., electric field, polarization, and electric displacement) in the simulation of ferroelectric, magnetoelectric, and piezoelectric materials [28–30]. These methods now allow to systematically and accurately explore both strain and electrostatic effects at the level of the individual bulk material. In particular, by calculating the ground state of a given compound as a function of the in-plane strain and out-of-plane electric displacement, one can trace two-dimensional maps that comprehensively describe *all configurations* that are, in principle, accessible in a superlattice geometry, i.e., at arbitrary electrical and mechanical boundary conditions.

Among the variety of materials that have been considered as building blocks for ferroelectric superlattices, perovskite-structure  $PbTiO_3$  (PTO) and  $BiFeO_3$  (BFO) occupy a special place. Indeed, the former is the end member of the  $Pb_xZr_{1-x}TiO_3$  family, the technologically most important piezoelectric material, while the latter is the most intensely studied of all naturally occurring multiferroics. Interestingly, even if both materials present active (and strong) FE and AFD instabilities in their cubic reference phase, their ground state remarkably differs. On one hand, PTO condenses in a purely ferroelectric  $P4mm$  phase, where the AFD instability has been suppressed by the large polar distortion. (FE and AFD modes generally, although not always [6,7], compete). Note that the AFD modes, even if they are absent in the low-temperature bulk phase, have been shown to play an important role in the ferroelectric  $\rightarrow$  paraelectric phase transition [31] and are predicted to become active in thin films at medium to large values of the epitaxial strain [32]. Bulk BFO, on the other hand, adopts a rhombohedral ( $R3c$ ) structure where a large polarization and antiphase AFD distortions [both oriented along the pseudocubic (111) direction] coexist. The balance between polar and nonpolar instabilities is extraordinarily subtle in this latter material, leading to a rich and complex energy landscape with many local minima [33]. In fact, numerous phase transitions driven by pressure [34], temperature [35–37], and epitaxial strain [19,38] have been recently predicted and observed in BFO. Given the extraordinarily rich behavior of both materials, it is hardly surprising that their combination results in an even broader variety of original phenomena. Indeed, recent *ab initio* simulations have shown that epitaxial short-period superlattices made of  $PbTiO_3$  and  $BiFeO_3$  layers may exhibit strain-driven isostructural phase transitions, exotic metastable phases, and unusually large oxygen octahedra tilts [32,39,40]. In view of the great fundamental and technological interest of bulk PTO, BFO, and layered heterostructures comprising both species, a detailed knowledge of how mutually coupled FE and AFD degrees of freedom in these materials respond to external electric fields and/or mechanical constraints is highly desirable.

In this article, we present a systematic first-principles study of the energy, structural, and dielectric properties of “bulk” [41] PTO and BFO as a function of *both* in-plane epitaxial strain ( $a$ ) and out-of-plane electric displacement field ( $D$ ). Our computational results are presented in the form of two-dimensional ( $a, D$ ) maps, which describe the structural and electronic ground state of the material at an arbitrary choice of the electrical and mechanical boundary conditions. These maps provide a comprehensive overview of *all* the phases

of BFO and PTO that can be realized via strain engineering and electrostatic coupling, i.e., by growing the material in a thin-film or superlattice form. Most importantly, these maps illustrate how the main functional properties (e.g., dielectric, piezoelectric) of either material evolve as a function of  $(a, D)$  and thus constitute an invaluable guide in the experimental search for new artificial materials. For instance, we identify the specific regions of the phase diagram where PTO or BTO display an unusual dielectric and structural softness, leading to very large dielectric and piezoelectric responses. For PTO, this region is located at small positive strain, where the polarization abruptly rotates from out-of-plane to in-plane. (Interestingly, in a very small range of in-plane strain values, we find a stable monoclinic structure, where the polarization has both in-plane and out-of-plane components and is accompanied by an out-of-phase AFD tilt mode). In the case of BFO, such a structural softness occurs in the orthorhombic  $Pmc2_1$  phase that becomes stable at high tensile strain, and whose existence was recently predicted by means of first-principles calculations [32,39].

In addition to their practical interest, our results also provide a wealth of valuable insight into the physics of either material, especially regarding the mutual interplay of strain, polarization, and AFD tilts. In this context, parallel to rationalizing the results of earlier works on PTO- and BFO-based systems [3,32,39], we could identify a notable case where the main order parameters do not follow the typical behavior that has been traditionally assumed in phenomenological theories. In particular, both PTO and BFO are characterized, at high tensile strain, by an in-phase out-of-plane AFD mode, whose amplitude *grows*, rather than decreasing, when an out-of-plane electric field (of arbitrary strength) is applied. This is in stark contrast with the expected trends (AFD modes usually tend to compete with the polar degrees of freedom) represented in Fig. 1(b).

This work is organized as follows: In Sec. II we provide the details of the computational strategy and *ab initio* methods that we used in the construction of the  $(a, D)$  diagrams. In Sec. III, we present our results and discuss them extensively. Finally, we conclude by summarizing our main findings in Sec. IV.

## II. COMPUTATIONAL DETAILS

### A. Construction of the $(a, D)$ maps

Our calculations are performed within the local spin density approximation to density-functional theory, as implemented in the “in-house” LAUTREC code. We apply a Hubbard  $U = 3.8$  eV to the Fe ions [32,42]. In all the simulations, we use the 20-atom  $\sqrt{2} \times \sqrt{2} \times 2$  simulation cell depicted in Fig. 1(c), which allows for reproducing the ferroelectric and antiferrodistortive distortions of interest [i.e., in-phase AFD<sup>+</sup> and out-of-phase AFD<sup>-</sup>, see Fig. 1(a)].

It is worth noting that working at fixed electric displacement  $D$  is in many respects analogous to working at fixed electric field  $E$ . At fixed  $D$ , however, a much broader range of configurations can be explored in FE materials, including regions of parameter space where the system is unstable with respect to a polar distortion [30,43]. Controlling  $D$  is akin to controlling  $P$  and therefore provides an intuitive and direct

conceptual link to phenomenological descriptions (i.e., Landau theory) where  $P$  is treated as the main order parameter.

Atomic and cell relaxations are performed by constraining the value of the out-of-plane component of  $D$  [30] and the two in-plane lattice vectors  $\mathbf{a}_1$  and  $\mathbf{a}_2$  (see Fig. 1). In the remainder of this article,  $D$  will denote the out-of-plane component of the electric displacement vector. Small tolerances of 0.005 eV/Å and 0.001 Kbar are imposed on the atomic forces and stresses. We correct for the bias deriving from the Pulay stress in the out-of-plane direction,  $\pi_P$ , by introducing a compensating  $-\pi_P \Omega$  term (where  $\Omega$  is the cell volume) in the expression of the internal energy. The calculations are repeated in order to span the physically relevant space defined by the set of parameters  $(a, D)$ .

In order to achieve an accurate description of the energy and structural properties of PTO and BFO in the  $3.6 \leq a \leq 4.2$  Å and  $0 \leq D \leq 1.5$  e/S intervals, we carry out explicit calculations on a fine regular grid of  $(a, D)$  points, spaced by  $\Delta a = 0.05$  Å and  $\Delta D = 0.1$  e/S (where  $e$  is the electron charge and  $S$  the surface of the five-atom unit cell). Spline interpolations are subsequently applied to the calculated data points in order to obtain smooth two-dimensional maps (see Figs. 3–7).

### B. Electrostatic and distortion analysis

The components of the total polarization in each relaxed configuration, i.e., in-plane  $\mathbf{P}_{\parallel} = (P_x, P_y)$  and out-of-plane  $P_z$ , were computed with the formula

$$P_{\alpha} = \frac{1}{\Omega} \sum_{\kappa\beta} Z_{\kappa\beta\alpha}^* u_{\kappa\beta}, \quad (1)$$

where  $\Omega$  is the volume of the cell,  $\kappa$  runs over all the atoms there,  $\alpha, \beta = x, y, z$  represent Cartesian directions,  $\mathbf{u}_{\kappa}$  is the displacement vector of the  $\kappa$ -th atom as referred to the cubic perovskite phase, and  $Z_{\kappa}^*$  the Born effective charge tensor calculated in the paraelectric reference state. We note that since both PTO and BFO materials are good ferroelectrics, one can regard the out-of-plane component of the total polarization,  $P_z$ , to be approximately equal to  $D$ .

The magnitude of the antiferrodistortive AFD<sub>*z*</sub><sup>+</sup>, AFD<sub>*z*</sub><sup>-</sup> (both with the rotation axis oriented along [001]) and AFD<sub>*xy*</sub><sup>-</sup> (with [110] axis) rotations were evaluated by considering the projection of the  $\mathbf{u}_{\kappa}$  vectors on the corresponding zone-boundary eigenmode, see Fig. 1(a). (We use a “+” or a “-” symbol to indicate in-phase and out-of-phase tilt modes, respectively).

### C. Computation of functional properties

The availability of the full  $(a, D)$  maps for a given material allows us to extract important functional properties (e.g., dielectric and piezoelectric coefficients) in a straightforward way as a by-product of our calculations [30]. In particular, the inverse dielectric constant of the system,  $\epsilon^{-1}$  (by  $\epsilon$  without subscripts we shall always imply the 33 components of the dielectric tensor), adopts the simple form

$$\epsilon^{-1} = \frac{4\pi}{\Omega} \frac{d^2 U}{dD^2}, \quad (2)$$

where  $U$  is the internal energy,  $\Omega = Sc$  the unit cell volume,  $S$  the unit cell surface, and  $c$  the unit cell out-of-plane parameter. Also, the *longitudinal* piezoelectric coefficient is readily obtained as

$$d_{33} = \frac{dc}{dV} = \left( \frac{dV}{dD} \right)^{-1} \frac{dc}{dD} = \frac{\epsilon}{c} \frac{dc}{dD}, \quad (3)$$

where  $V = \frac{4\pi}{S} \frac{dU}{dD}$  is the potential drop across the unit cell in the  $z$  direction [30]. Likewise, the *shear* piezoelectric coefficient is expressed within our formalism as

$$d_{35} = \frac{dw}{dV} = \left( \frac{dV}{dD} \right)^{-1} \frac{dw}{dD} = \frac{\epsilon}{c} \frac{dw}{dD}, \quad (4)$$

where  $w$  corresponds to the projection of the  $\mathbf{a}_3$  lattice vector on the basal plane defined by  $\mathbf{a}_1$  and  $\mathbf{a}_2$  (see Fig. 1). (The Voigt notation of the shear strain, therefore, refers to the rotated axes of the 20-atom cell and not to the pseudocubic axes).

The response coefficients defined in Eq. (2), Eq. (3), and Eq. (4) are directly related to those discussed by Wu, Vanderbilt, and Hamann (WVM) [44]. In particular, the dielectric constant of Eq. (2) corresponds to the free-stress permittivity of WVM,  $\epsilon_{33}^{(\sigma)}$ . Regarding the  $d_{\alpha\beta}$  tensor, our notation is consistent with WVM. It is useful for later use (again, following WVM) to introduce the fixed- $D$ , free-stress piezoelectric coefficients

$$g_{33} = \frac{1}{c} \frac{dc}{dD}, \quad g_{35} = \frac{1}{c} \frac{dw}{dD}, \quad (5)$$

which trivially relate to the corresponding component of the  $\mathbf{d}$  tensor as  $d_{\alpha\beta} = \epsilon g_{\alpha\beta}$ .

Note that the above definitions can be readily used to predict the dielectric and piezoelectric properties of a multicomponent system (e.g., a layered superlattice) based on the bulk properties of the constituents. For example, consider a superlattice (SL) with a total thickness  $t_A$  of material A and  $t_B$  of material B. In this case, one has

$$\begin{aligned} \frac{t_A + t_B}{\epsilon^{\text{SL}}} &= \frac{t_A}{\epsilon^A} + \frac{t_B}{\epsilon^B}, \\ (t_A + t_B)g^{\text{SL}} &= t_A g^A + t_B g^B. \end{aligned} \quad (6)$$

As above, one can then easily recover the overall  $d$  coefficients as  $d^{\text{SL}} = \epsilon^{\text{SL}} g^{\text{SL}}$ .

### III. RESULTS AND DISCUSSION

#### A. Bulk PbTiO<sub>3</sub>

In Fig. 2, we show a schematic phase diagram of PTO, calculated as a function of  $(a, D)$ , while in Fig. 3 we report a series of detailed 2D maps that illustrate the evolution of most relevant structural and electrical degrees of freedom within the same  $(a, D)$  range. For each region of the phase diagram (Fig. 2) we indicate the space group of the stable crystal phase therein and we mark the resulting two-phase boundaries as a dashed line. (The same phase boundaries are also shown in the maps of Fig. 3). Moving from smaller to larger values of  $a$ , the dashed lines correspond, respectively, to the suppression of  $\text{AFD}_z^-$  tilts, the onset of  $P_{xy}$ , and the onset of  $\text{AFD}_z^+$  rotations (see Fig. 3). We note that, according to our calculations, all the phase transitions occurring in PTO are of second-order type,

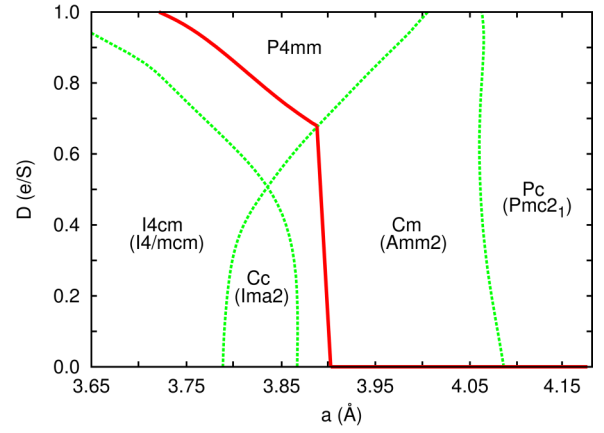


FIG. 2. (Color online) Calculated phase diagram of PbTiO<sub>3</sub> as a function of the in-plane lattice parameter and out-of-plane electric displacement. The thick red line joins the states of minimum energy obtained at fixed  $a$ , and the dashed green lines represent two-phase boundaries involving second-order phase transitions (see text). Space groups quoted within parentheses correspond to crystal structures found at  $D = 0$ .

i.e., the energy of the crystal varies continuously while specific distortions—FE, AFD, or both simultaneously—emerge or are suppressed. The solid red line in Figs. 2 and 3 indicates, for each value of  $a$ , the value of  $D$  that minimizes the energy; the points of this curve therefore correspond to the electrostatic equilibrium configurations as a function of the in-plane strain. Note that  $P_z$  exactly coincides with  $D$  along such path, as at the stationary points of the  $U(D)$  curve the macroscopic electric field vanishes by definition. The curve mostly follows the known trends for PTO thin films [32,39]: (i) A zero or negative in-plane strain favors a tetragonal  $P4mm$  state with a strong out-of-plane component of the polarization,  $P_z$ . PTO remains in the tetragonal  $P4mm$  phase down to  $a = 3.60$  Å, where the resulting  $c/a$  ratio and out-of-plane polarization become very large (1.35 and 1.36 C/m<sup>2</sup>, respectively). (ii)  $P_z$  is suppressed upon application of a tensile strain, whereby the polarization aligns with the in-plane (110) direction (the orientation of the polarization abruptly changes from [110] to [001] at  $a = 3.90$  Å) and the system transitions to the orthorhombic  $Amm2$  phase. This is analogous to the phase occurring in BaTiO<sub>3</sub> under similar conditions [45]. (iii) Finally, at a large-enough value of the tensile strain a second phase transition occurs, where an  $\text{AFD}_z^+$  mode appears; as a consequence, the symmetry of the system reduces to  $Pmc2_1$  as recently reported in Refs. [32,39].

While the behavior described above is fully consistent with the results of earlier studies we found, however, some interesting surprises as well. First, we find a stable monoclinic  $Cm$  phase in the narrow  $3.89 \leq a \leq 3.91$  Å interval. This phase is characterized by  $P_z, P_{xy} \neq 0$  and  $\alpha \neq 90^\circ$  (see Fig. 4) and, to our knowledge, has never been predicted or observed previously. (The energy difference between the monoclinic  $Cm$  and orthorhombic  $Amm2$  phases is very small, i.e., 1–2 meV/f.u., which explains why the monoclinic structure might have been missed in earlier studies). Second, our calculated phase diagram of Fig. 2 clearly shows that  $\text{AFD}_{xy}^-$  distortions do not occur in PTO at any value of  $a$  or  $D$ . Earlier

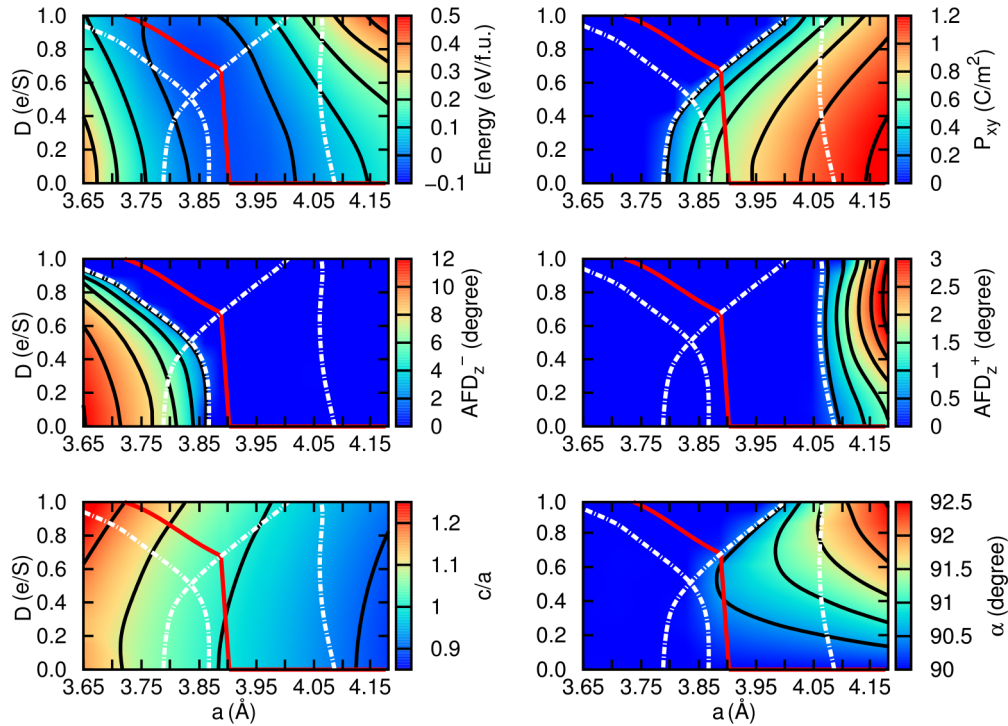


FIG. 3. (Color online) Calculated energy and structural properties of PTO expressed as a function of  $a$  and  $D$ .  $\alpha$  is the monoclinic angle, i.e., that formed by the  $\mathbf{a}_3$  and  $\mathbf{a}_1 + \mathbf{a}_2$  vectors in the relaxed unit cell;  $P_{xy}$  the in-plane polarization (oriented along the [110] direction);  $c/a$  is the axial ratio  $|\mathbf{a}_3|/(\sqrt{2}a)$ . Solid black curves are isolines connecting the states that share a common value for a given property, and the thick red curves joins the states at electrostatic (but not necessarily mechanical) equilibrium. The dashed white lines match the dashed green curves of Fig. 2, and indicate second-order phase boundaries.

studies in the literature [32,39,46] predicted such distortions to occur in the tensile-strain region, where the polarization vector has an in-plane orientation. (These structures were, therefore, identified as orthorhombic  $Ima2$  rather than  $Amm2$ ). This discrepancy can be rationalized by observing that the  $AFD_{xy}^-$  mode amplitude was found [32,39,46] to be very small (i.e.,  $\sim 1^\circ$ ), which implies that that the  $Amm2$  and  $Ima2$  phases

are essentially degenerate in energy. Whether they show up in a calculation might therefore depend on subtle details of the numerical implementation.

Now we shall discuss more in detail the results that we obtained by exploiting the full capabilities of our computational approach, i.e., by imposing arbitrary  $(a, D)$ , and including those configurations that are characterized by a nonzero internal field along the  $z$  direction.

First, it is interesting to note the unusually flat potential-energy landscape in a vicinity of the zero-strain equilibrium state (see Fig. 3); this indicates that the system is extremely sensitive to external perturbations in this region of the phase diagram. Indeed, recall that in the orthorhombic  $Amm2 \rightarrow$  tetragonal  $P4mm$  transition the polarization abruptly rotates from in-plane to out-of-plane; thus, large dielectric and piezoelectric responses are expected to occur near  $a = 3.90 \text{ \AA}$  (we will comment more extensively on this point in Sec. III C).

The structurally most complex region of the phase diagram occurs in the moderately compressive strain regime ( $3.79 \leq a \leq 3.87 \text{ \AA}$ ) and  $D$  values that are smaller than the equilibrium  $P_z$ . Here all the most important structural modes of PTO ( $P_{xy}$ ,  $P_z$ , and  $AFD_z^-$  distortions) coexist, and the symmetry of the crystal is monoclinic  $Cc$  (see Figs. 2 and 3). (It reduces to orthorhombic  $Ima2$  at  $D = 0$ ). The occurrence of the  $P_{xy}$  and  $AFD_z^-$  distortions, which are active instabilities of the reference  $P4/mmm$  structure but are absent in the zero-field equilibrium phase within this strain interval, may appear surprising. This, however, can be easily rationalized in terms of the mutual competition between different instabilities in PTO. At

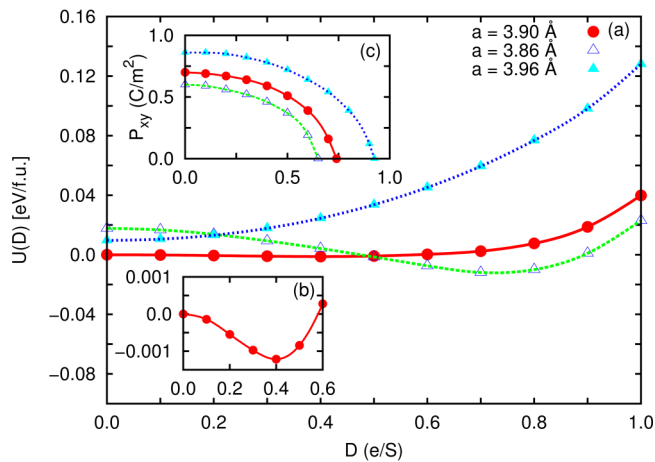


FIG. 4. (Color online) (a) Calculated energy curves in PTO at three different in-plane parameters and expressed as a function of the electric displacement. (b) Close-up of the energy function computed in the monoclinic  $Cm$  phase. (c) In-plane polarization expressed as a function of  $D$  at the three selected in-plane strain values.

zero electric field (i.e., red curves in Figs. 2 and 3),  $P_z$  is large enough to prevail over the other degrees of freedom, which are completely suppressed. By reducing  $P_z$  (as can occur, in practical situations, as a consequence of depolarizing field effects), the aforementioned cross-couplings are weakened, allowing the competing  $P_{xy}$  and  $AFD_z^-$  distortions to reenter the ground-state structure. This finding explains the results of a recent study [3], where a superlattice geometry was found to induce a monoclinic structure analogous to that described here in the PTO layers. Our results indicate that the electrical boundary conditions are, in fact, likely to be the main cause for such an outcome. Higher in-plane compression ( $a \leq 3.79 \text{ \AA}$ ) suppresses the in-plane polarization instabilities completely, and at the same time increase the strength of  $AFD_z^-$  rotations; the symmetry of the crystal is tetragonal  $I4cm$  (tetragonal  $I4/mcm$  at  $D = 0$ ). Our data suggest that the  $AFD_z^-$  rotations will consistently show up at arbitrary (moderate to strong) compressive strain values, provided that a depolarizing effect is present.

In the moderate tensile strain regime ( $3.90 \leq a \leq 4.09 \text{ \AA}$ ), all oxygen octahedral rotations are suppressed and the symmetry of the system is monoclinic  $Cm$ . (This corresponds to a polarization oriented along  $[uvv]$ , with  $v < u$ , where the out-of-plane component can be induced by applying an out-of-plane electric field to the equilibrium  $Amm2_1$  phase). Finally, in the  $4.09 \leq a \leq 4.20 \text{ \AA}$  interval, the monoclinic angle  $\alpha$  increasingly deviates from  $90^\circ$  as  $D$  is increased, and the  $AFD_z^+$  rotations become more prominent. Note that, as  $P_z$  increases, the in-plane component of the polarization becomes smaller (although full suppression of  $P_{xy}$  is not observed). These features are consistent with a monoclinic  $Pc$  phase that is closely related to the equilibrium orthorhombic  $Pmc2_1$  found at  $D = 0$ . We note that the trend observed in this region is quite surprising: As  $P_z$ , or, equivalently,  $D$ , increases the  $AFD_z^+$  rotations become larger. This contrasts with the typical trends shown in Fig. 1. (We already pointed out that such a trend was indeed followed by the  $AFD_z^-/P_{xy}$  modes in the compressive regime). Thus, a cooperative rather than a competitive coupling appears to be operating between the  $P_z$  and  $AFD_z^+$  degrees of freedom. This observation points to new interesting opportunities for tuning of the  $AFD_z^+$  oxygen rotations via application of an external electric field.

### B. Bulk BiFeO<sub>3</sub>

For the case of BFO, we shall present our results by following a similar strategy to what we did in the PTO case: The overall phase diagram is shown in Fig. 5, while Figs. 6 and 7 illustrate the detailed behavior of the individual degrees of freedom. (We split the relevant parameter space into two parts here to better describe the large compressive strain region, where the spontaneous polarization adopts very large values). We use the same convention as in Figs. 2 and 3 regarding the electrostatic equilibrium path and the two-phase boundaries, with the only difference that, in contrast to the PTO case, the latter are almost always shown as solid lines here. This reflects an important outcome of our calculations: Most phase boundaries in BFO turn out to be of the first-order type. (The only exception is the transition to the  $P4mm$  state at very small values of  $a$ , marked in the upper left corner of Fig. 5).

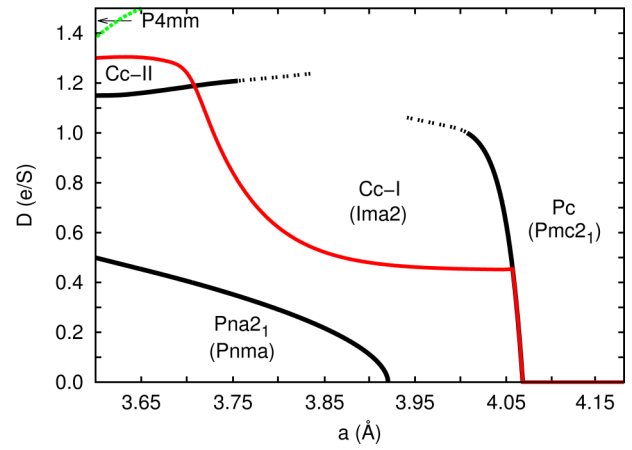


FIG. 5. (Color online) Calculated phase diagram of BiFeO<sub>3</sub> as a function of the in-plane lattice parameter and out-of-plane electric displacement. The thick red line joins the states of minimum energy obtained at fixed  $a$ , and the solid black (dashed green) lines represent two-phase boundaries involving first-order (second-order) phase transitions. Space groups quoted within parentheses correspond to crystal structures obtained at  $D = 0$ . Dotted black lines indicate extrapolation.

As before, the path described by the  $E_z = 0$  states (minimum energy configurations at a given value of  $a$ ) is consistent with the results of earlier works [32,39]: (i) For a large range of in-plane strain values around the equilibrium parameter, BFO adopts a monoclinic  $Cc$  (we shall indicate this phase as  $Cc$ -I) state that is closely related to the bulk rhombohedral ground state. Here both the polarization and the  $AFD^-$  vector are large and roughly oriented along the (111) pseudocubic direction. Their evolution with decreasing  $a$  follows the usual trend:  $P_z$  and  $AFD_z^-$  display a progressive enhancement, while the in-plane components of both degrees of freedom simultaneously decrease in amplitude. (ii) At a sufficiently large compressive strain ( $a = 3.85 \text{ \AA}$ ), the  $AFD_z^-$  distortion amplitude peaks and then rapidly falls to zero, while both the  $c/a$  ratio and  $P_z$  undergo a drastic increase. (At  $a = 3.65 \text{ \AA}$ , for instance, the value of  $P_z$  is  $1.56 \text{ C/m}^2$  and  $c/a = 1.28$ ). We identify this abrupt change with the isosymmetric [47] transition to the well-known *supertetragonal* phase of BFO (also known in the literature as “T-like”) that was experimentally observed in epitaxial films under a large compressive strain [19,38]. (iii) At the other extreme end of the phase diagram (i.e., in the strongly tensile regime,  $a > 4.07 \text{ \AA}$ ) BFO stabilizes in an orthorhombic  $Pmc2_1$  phase, in all respects analogous to the  $Pmc2_1$  structure that occurs in PTO at similarly large strain values (see previous section).

When we move away from the electrostatic equilibrium curve, BFO reveals a number of remarkable (and potentially useful) features, as we shall illustrate in the following. In the zero or mildly compressive strain regime ( $a \leq 3.92 \text{ \AA}$ ) we observe at small  $D$  values a region where BFO adopts an orthorhombic  $Pna2_1$  structure. This state exhibits very large  $AFD_z^+$  and  $AFD_{xy}^-$  O<sub>6</sub> rotations, and a nonzero  $P_z$ . The latter, however, is not “ferroelectric” in the usual sense: The system here behaves like a nonlinear dielectric, with a metastable local minimum at  $D = 0$ , where the symmetry becomes

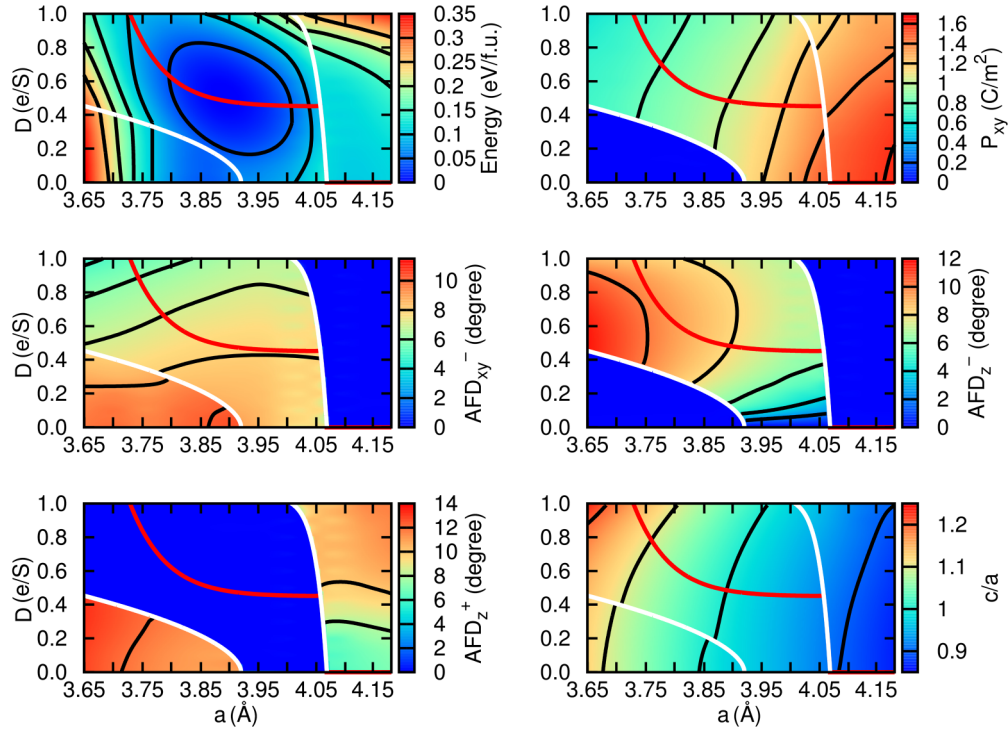


FIG. 6. (Color online) Calculated energy and structural properties of BFO expressed as a function of  $a$  and  $D$ . Solid black curves are isolines, and the thick red line joins the states of minimum energy (zero electric field) at a given in-plane  $a$ . Thick white curves indicate first-order phase transitions.

orthorhombic  $Pnma$ . We can thus expect that under a strong depolarizing field (and conditions that prevent domain formation) a BFO film might adopt a  $Pnma$  ground state, which was so far only observed in bulk at high pressure [48]. As  $a$  is

decreased, the  $D$  interval over which this orthorhombic phase occurs becomes broader, while the amplitude of the  $AFD_{z}^{+}$  and  $AFD_{xy}^{-}$  oxygen rotations remain practically unchanged. At even larger compressive strains ( $3.60 \leq a \leq 3.65$  Å) we find

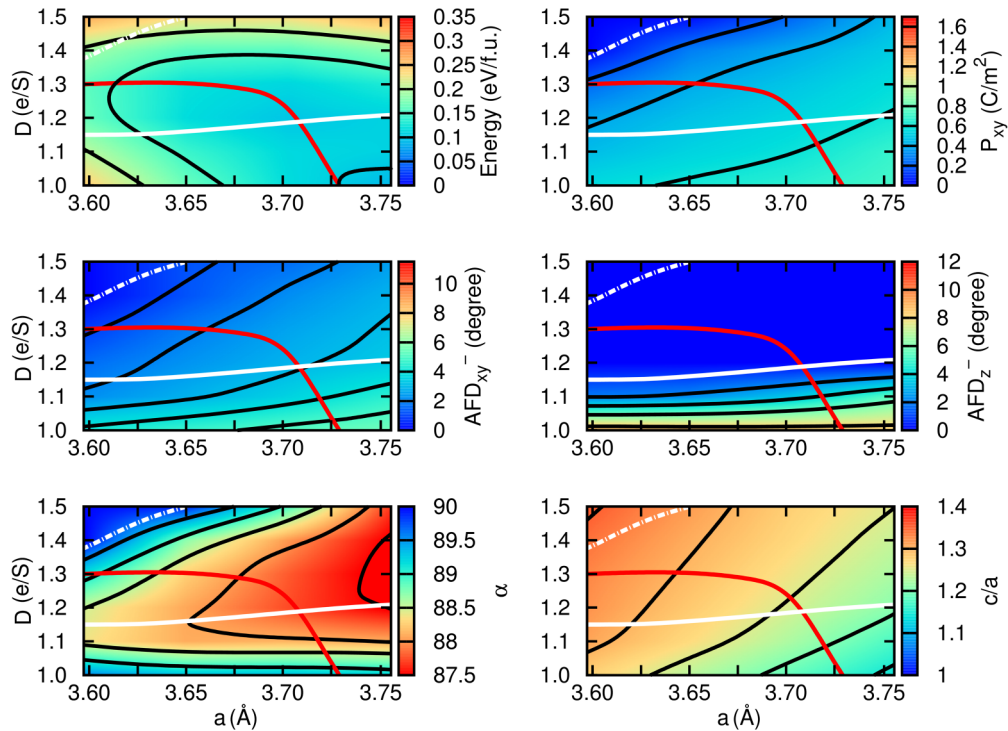


FIG. 7. (Color online) Same as in Fig. 6 but considering smaller (larger)  $a$  ( $D$ ) values.

a new region, this time at *large* values of  $D$ , where the  $\text{AFD}_{xy}^-$  oxygen octahedral rotations and in-plane polarization completely disappear and the crystal becomes tetragonal  $P4mm$ . According to our calculations, the electric field-induced monoclinic  $Cc-II \rightarrow$  tetragonal  $P4mm$  transformation is of second-order type. Note that this same  $P4mm$  phase could be, in principle, obtained even without the application of an electric field by further compressing the crystal in-plane [39]. However, the strain that one would have to apply is enormous ( $a \leq 3.60 \text{ \AA}$ )—our calculations show that by *combining* the effects of in-plane compression and out-of-plane electric field, one might have better chances of experimentally stabilizing the high-energy  $P4mm$  phase, which is probably out of reach if one relies solely on mechanical means. Finally, moving now to the large tensile strain region ( $a > 4.07 \text{ \AA}$ ), BFO adopts the same monoclinic  $Pc$  phase that we have found in PTO under similar conditions (see Sec. III A). Also in this case it is interesting to note that the  $\text{AFD}_z^+ \text{O}_6$  rotations become larger in amplitude as  $D$ , and, consequently,  $P_z$ , is increased. Remarkably, the potential energy surface around  $D = 0$  appears to be rather flat, which indicates a very large dielectric polarizability; this has important implications for practical applications, as we shall discuss shortly in Sec. III C.

### C. Functional properties

The results described above have direct implications over the functional properties of the two materials, as we shall see in the following. We shall focus more specifically on the dielectric and piezoelectric properties, whose dependence on the external parameters will be again illustrated in the form of 2D maps. We shall discuss the two materials separately, starting with  $\text{PbTiO}_3$ .

#### 1. Bulk $\text{PbTiO}_3$

In Fig. 8(a), we show the calculated inverse dielectric constant,  $\epsilon^{-1}$ , of bulk PTO in the region of parameter space spanned by  $3.6 \leq a \leq 4.2 \text{ \AA}$  and  $0 \leq D \leq 1.0 \text{ e/S}$ . First, note the blank area in the lower left corner of the graph; it corresponds to  $(a, D)$  points where  $\epsilon^{-1}$  adopts negative values, pointing to an instability of the system towards a ferroelectric distortion. As these points are experimentally inaccessible, we have decided to exclude them from our analysis. The most interesting region in the  $(a, D)$  map is that where the crystal, under zero-field conditions, transitions (for increasing  $a$ ) from the orthorhombic  $Amm2$  to the tetragonal  $P4mm$  phase via the intermediate monoclinic  $Cm$  phase (see Sec. III A). Here in the  $3.90 \leq a \leq 3.94 \text{ \AA}$  interval, for instance,  $\epsilon$  adopts values which are higher than  $\sim 500$  (in units of  $\epsilon_0$ , that is, the dielectric constant of vacuum) in the corresponding zero-field states (indicated with a magenta line). The  $Amm2 \rightarrow P4mm$  phase transition corresponds to an abrupt rotation of the polarization vector from in-plane to out-of-plane, and thus the large dielectric response of the system in that region stems from the flatness of the potential landscape that governs  $P_z$ . Indeed, in the tensile-strain regime the system behaves as a normal dielectric along  $z$ , i.e., the internal energy of the system  $U(D)$  depends quadratically on  $D$ . Conversely, in the compressive regime,  $U(D)$  adopts a symmetric double-well form (see Fig. 4). In crossing the boundary,  $U(D)$  flattens significantly

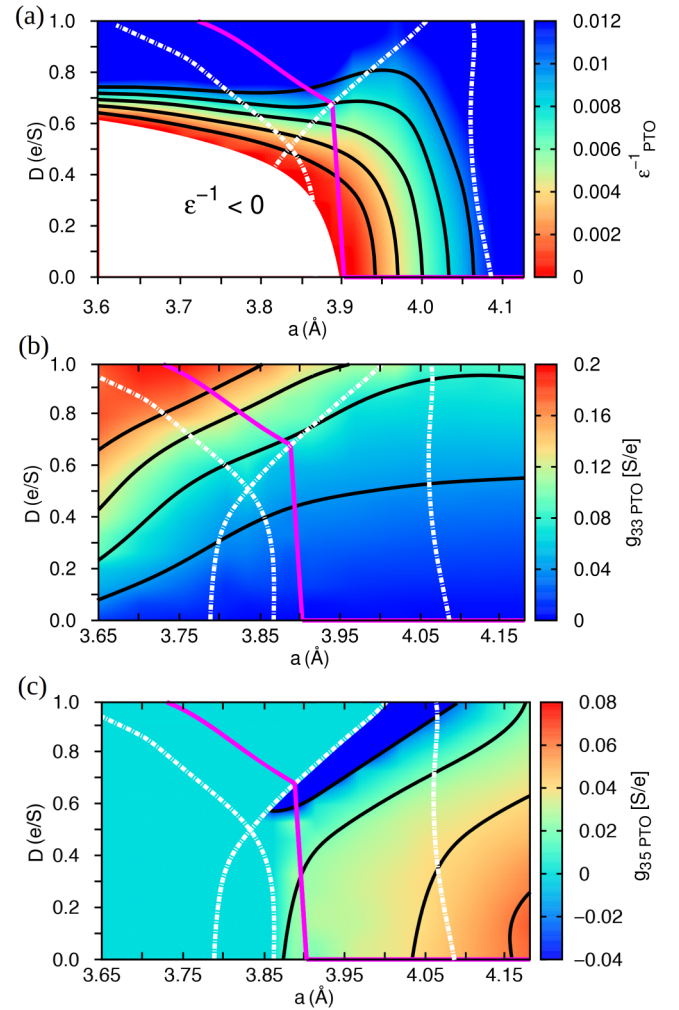


FIG. 8. (Color online) Inverse dielectric constant  $\epsilon^{-1}$  (a) and fixed- $D$  piezoelectric coefficients  $g_{33}$  (b) and  $g_{35}$  (c), calculated in PTO and expressed as a function of  $a$  and  $D$ . The instability region wherein the dielectric constant would be negative is not shown (a). The magenta solid line joins the states of minimum energy at given  $a$ , and the dashed white lines mark the boundaries between different phases.

in the region near  $D = 0$ , where its second derivative, and, consequently,  $\epsilon^{-1}$ , becomes very small.

As they are directly proportional to  $\epsilon$ , the  $d_{33}$  and  $d_{35}$  piezoelectric coefficients of bulk PTO are expected to be giant [see Eqs. (3) and (4) in Sec. II C] in the transition region described above. Of course, a necessary condition is that the corresponding  $g_{33}$  and  $g_{35}$  coefficients do not vanish. Regarding the longitudinal  $g_{33}$  coefficient, Fig. 8(b) shows a relatively simple monotonous behavior, with a roughly linear increase from zero (at the  $D = 0$  state, where it vanishes by symmetry) to 0.08–0.20 (depending on the strain state) at the highest values of  $D$ . (Interestingly, the rate of increase of  $g_{33}$  with  $D$ , which can be regarded as an effective electrostrictive coefficient, seems to be rather sensitive to the in-plane strain, being largest in the extreme compressive regime, and milder under tensile conditions). By combining the information of  $\epsilon^{-1}$  and  $g_{33}$ , one can draw the following conclusions: (i)  $d_{33}$

vanishes at tensile strain by symmetry, unless a sufficiently large electric field is applied to the crystal. (ii)  $d_{33}$  is nonzero but relatively small in the compressive strain regime, where the zero-field curve lies far from the region where  $\epsilon$  diverges. (One can, in principle, try to approach that region by applying an  $E$ -field antiparallel to  $P_z$ , although the crystal will likely switch to the opposite polarization state well before reaching it). (iii) In the intermediate region where PTO is either monoclinic or tetragonal (but close to the phase boundary),  $d_{33}$  becomes giant as speculated above, due to the structural and dielectric softness of the system therein.

As for the *shear* piezoelectric coefficient,  $g_{35}$  [see Fig. 8(c)], we find a very rich behavior that is remarkably sensitive to the mechanical and electrical boundary conditions. First, note that whenever  $P_{xy}$  vanishes (i.e., at compressive strain),  $g_{35}$  vanishes because of symmetry (the crystal axes form orthogonal angles with no shear). The physically interesting region occurs from zero to moderately tensile strain, where the in-plane components of the polarization start being active. Surprisingly, the  $g_{35}$  coefficient shows a rather peculiar behavior: It is positive in most of the region of parameter space where  $P_{xy}$  is nonzero (this includes all equilibrium zero-field states with  $Amm2$  symmetry, occurring at  $a > 3.90 \text{ \AA}$ ), except for a narrow region close to the phase boundary where it becomes *negative*.

In order to understand the physical origin of this result, it is useful to recall the form of the coupling terms in the free energy that involve polarization and shear strain. At the lowest order, in PTO such a coupling is governed by [49]

$$E_{\text{coupl}} = AP_z P_{xy} \sigma_{\text{shear}}, \quad (7)$$

where  $\sigma_{\text{shear}}$  is the corresponding component of the stress tensor (note that the shear occurs between the out-of-plane [001] and in-plane [110] axes) and  $A$  is the coupling coefficient. The  $g_{35}$  piezoelectric coefficient can be roughly estimated by deriving the above coupling term twice with respect to  $P_z$  (which in the context of our calculations essentially corresponds to  $D$ ) and  $\sigma_{\text{shear}}$ ,

$$g_{35} \sim \frac{\partial^2 E_{\text{coupl}}}{\partial P_z \partial \sigma_{\text{shear}}}. \quad (8)$$

It is useful, for analysis purposes, to break down the above equation into two intermediate steps by introducing the shear strain,  $\epsilon_{\text{shear}}$ ,

$$\epsilon_{\text{shear}} \sim \frac{\partial E_{\text{coupl}}}{\partial \sigma_{\text{shear}}}, \quad g_{35} \sim \frac{\partial \epsilon_{\text{shear}}}{\partial P_z}. \quad (9)$$

One has, trivially,

$$\epsilon_{\text{shear}} \propto P_z P_{xy}. \quad (10)$$

This behavior of  $\epsilon_{\text{shear}}$ , which corresponds to the deviation of the monoclinic angle  $\alpha$  from  $90^\circ$ , is qualitatively well reproduced in our calculations (see Fig. 3). From the evolution of  $\alpha$  as a function of  $D$  (for a fixed  $a$ ), one can immediately appreciate the origin of the sign change in  $g_{35}$ : Close to  $D = 0$ ,  $\alpha$  grows linearly with  $D$  (i.e., its derivative with respect to  $D$  is positive), reaches a peak, and then rapidly drops back (negative region) to zero when approaching the phase boundary.

In a close vicinity of such boundary,  $P_z$  has a finite value and therefore can be approximated by a constant; one should then have

$$\epsilon_{\text{shear}} \propto P_{xy}. \quad (11)$$

Now, since the transition is of second-order type, for a given  $a$  one expects a critical behavior of  $P_{xy}$  with respect to  $D$  of the form

$$P_{xy} \propto \sqrt{D_0(a) - D}, \quad (12)$$

where  $D_0(a)$  describes the phase boundary. By combining Eq. (11) and Eq. (12), and by further taking the first derivative in  $D$ , one obtains that the piezoelectric coefficient  $g_{35}$  *diverges* at the boundary as

$$g_{35} \propto -\frac{1}{\sqrt{D_0(a) - D}}. \quad (13)$$

Unfortunately, the divergence does not show up in our graphs because of the relatively coarse grid of  $(a, D)$  points that we have used to sample our parameter space. Nevertheless, the above conclusion is solid, as it stems from basic symmetry arguments and from the second-order nature of the phase transition. (The latter is unambiguously demonstrated by our numerical results). This points to a promising route to achieving a large piezoelectric response by tuning the  $D$  coefficient  $g_{35}$  rather than the dielectric constant. We expect this mechanism to be especially useful in superlattices, because of the additive property [see Eq. (6)] of the  $g$  coefficients. [Conversely, the dielectric constant obeys the typical series-capacitor model, Eq. (6), making it harder to enhance this latter functionality in a layered system].

## 2. Bulk BiFeO<sub>3</sub>

The calculated inverse dielectric constant of BFO, expressed as a function of the in-plane lattice parameter and out-of-plane electric displacement, is shown in Fig. 9(a). As in the PTO case, we have excluded from the graph the region where the system is unstable against a polar distortion and hence has a negative permittivity (white area). (In the region where BFO adopts the  $Pna2_1$  phase  $\epsilon^{-1}$  is in fact positive; however, for the sake of simplicity and because that region is experimentally difficult to access, we ignore it in the following analysis). The data points that lie closest to the white area are characterized by a vanishing value of  $\epsilon^{-1}$ , and hence by a diverging dielectric constant, which could be interesting for applications. At large tensile strain,  $\epsilon^{-1}$  presents some discontinuities, which occur more specifically along the  $Pmc2_1 \rightarrow Cc$ -I phase boundary. (Recall that the involved phase transformation is of first-order type and is characterized by a drastic structural change; this explains the abrupt jump in the response properties of the crystal). Interestingly, at  $a > 4.05 \text{ \AA}$  and for moderate values of  $D$  ( $0 \leq D \leq 0.5 e/S$ ), where the system is in a monoclinic  $Pc$  phase (orthorhombic  $Pmc2_1$  at  $D = 0$ ),  $\epsilon$  adopts very large values. In fact, the high-tensile strain  $Pmc2_1$  phase appears to be on the verge of having a polar instability along  $z$ . This fact reflects itself in an unusual flatness of the  $U(D)$  energy curves around  $D = 0$ , which in turn results into a very large dielectric (and

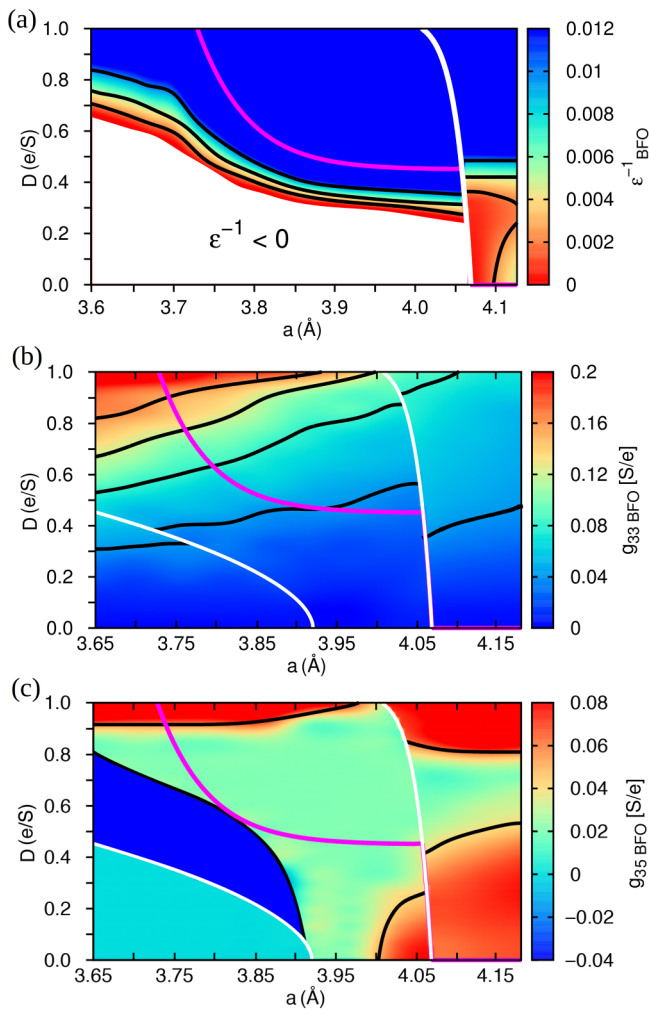


FIG. 9. (Color online) Inverse dielectric constant  $\epsilon^{-1}$  (a) and the fixed- $D$  piezoelectric coefficients  $g_{33}$  (b) and  $g_{35}$  (c) calculated in BFO and expressed as a function of  $a$  and  $D$ . The instability region wherein the dielectric constant would be negative is not shown (a). The magenta solid line joins the states of minimum energy at given  $a$ , and the solid white lines mark the boundaries between different phases.

piezoelectric, as we shall see shortly) response of the system [see Eq. (2)].

Regarding the *longitudinal* piezoelectric coefficient [see Fig. 9(b)],  $g_{33}$ , BFO behaves roughly like PTO:  $g_{33}$  is zero at  $D = 0$ , grows linearly for increasing  $D$ , and is largest in the upper left corner of the plot, i.e., at large compressive strain and large out-of-plane polarization. (Of course, the first-order phase transition lines and the corresponding discontinuities in  $g_{33}$  are absent in PTO; however, these do not produce a profound qualitative change in the overall picture). Note that, at difference with PTO, the system does not cross a state of marked structural softness at small applied strains [the zero-field line stays far away from the high- $\epsilon$  region unless a very large tensile strain is applied, while in PTO it crosses through it at  $a \sim 3.9 \text{ \AA}$ , see Fig. 8(a)]. Thus, as in the large tensile strain region  $g_{33}$  (and hence  $d_{33}$ ) vanishes by symmetry at zero electric field, we conclude that the transition from  $Cc$ -I to  $Cc$ -II (which occurs at large compressive strain) constitutes

the most promising configuration for obtaining an enhanced value of  $d_{33}$  in BFO.

The *shear* piezoelectric coefficient, on the other hand, displays a complex behavior that differs qualitatively from the PTO case and that does not lend itself to a comparatively simple physical interpretation [see Fig. 9(c)]. As a matter of fact, in BFO we have, in addition to the polarization-strain coupling that we mentioned in the previous section, a further term in the free energy that couples the strain to the AFD modes,

$$E_{\text{coupl}} = AP_z P_{xy} \sigma_{\text{shear}} + B \phi_z \phi_{xy} \sigma_{\text{shear}}, \quad (14)$$

where  $B$  is a second coupling coefficient and  $\phi_{z,xy}$  are the AFD $_{z,xy}^-$  distortion amplitudes. It is difficult, in the context of our calculations, to disentangle the effects of the two different coupling terms; for this reason, in the following we shall limit ourselves to commenting on the general trends that emerge from our data.

To start with, we note that the system in the proximity of zero epitaxial strain is characterized by small  $g_{35}$  values (the zero-field curve stay close to the  $g_{35} = 0$  isoline for a relatively wide range of in-plane lattice parameters). Again, only at rather extreme values of the epitaxial strain does the system become potentially interesting for piezoelectric applications. For example, at high compressive strains the shear angle shows a steep increase as a function of  $D$  (see Fig. 7), which results in a relatively large  $g_{35}$  coefficient. (Recall that in similar conditions the out-of-plane  $c$  parameter is also characterized by a strong dependence on  $D$ —this yields a large value of the longitudinal  $g_{33}$  coefficient, as we pointed out earlier). The most interesting region of parameter space in the present context, however, is by far the tensile strain one, where BFO adopts the  $Pmc2_1$  phase. Here a relatively large value of  $g_{35}$  is combined with a giant value of the out-of-plane dielectric constant,  $\epsilon$ ; this results in a  $d_{35}$  coefficient in excess of 700 pm/V at zero applied field.

#### IV. SUMMARY

We have studied the physical behavior of archetypal ferroelectrics  $\text{PbTiO}_3$  and  $\text{BiFeO}_3$  under arbitrary electrical and mechanical boundary conditions by means of state-of-the-art *ab initio* methods. Our calculations provide a detailed description of the complex interplay between polar and structural degrees of freedom in these materials over a comprehensive range of in-plane strain ( $a$ ) and out-of-plane electric displacement field ( $D$ ) values. Of particular relevance is the assessment and rationalization of the related dielectric and piezoelectric response functions, which can be naturally accessed as a by-product of our calculations.

In bulk PTO, we have predicted the existence of a new monoclinic  $Cm$  phase that is stable in a narrow strain interval and that bears important similarities to a previously reported structure in PTO-based superlattices. We have identified the regions in ( $a, D$ ) space wherein PTO exhibits a giant dielectric and piezoelectric response. In particular, we have unravelled a coupling mechanism by which its shear piezoelectric coefficient  $d_{35}$  diverges in reaching the monoclinic  $Cm$ –tetragonal  $P4mm$  phase boundary. In BFO, we have shown that a complex interplay between polar and antipolar distortions reigns in the region of high tensile strains wherein an orthorhombic  $Pmc2_1$

phase becomes stable. In that same region, we find that both the dielectric and shear piezoelectric responses of the system are extremely large.

While the present analysis has been based on bulk calculations, we emphasize that our findings are directly relevant to the the rational design of multicomponent ferroelectric superlattices, as our methodology allows one to accurately predict their functional properties based on the  $(a, D)$  maps of the bulk building blocks. In this sense, our study opens a promising new avenue in the ongoing search for new functional oxide systems with enhanced functionalities.

## ACKNOWLEDGMENTS

This research was supported by the Australian Research Council's Future Fellowship funding scheme (Project No. FT140100135), MINECO-Spain (Grants No. MAT2010-18113, No. CSD2007-00041, and No. FIS2013-48668-C2-2-P), and Generalitat de Catalunya (2014 SGR301). We thankfully acknowledge the computer resources, technical expertise, and assistance provided by RES, CESGA, and the Australian Government through Magnus under the National Computational Merit Allocation Scheme.

- 
- [1] R. E. Cohen and H. Krakauer, *Phys. Rev. B* **42**, 6416 (1990).  
 [2] R. E. Cohen, *Nature* **358**, 136 (1992).  
 [3] P. Aguado-Puente, P. García-Fernández, and J. Junquera, *Phys. Rev. Lett.* **107**, 217601 (2011).  
 [4] E. Bousquet, M. Dawber, N. Stucki, C. Lichtensteiger, P. Hermet, S. Gariglio, J.-M. Triscone, and P. Ghosez, *Nature (London)* **452**, 732 (2008).  
 [5] A. P. Levanyuk and D. G. Sannikov, *Sov. Phys. Uspekhi* **17**, 199 (1974).  
 [6] N. A. Benedek and C. J. Fennie, *Phys. Rev. Lett.* **106**, 107204 (2011).  
 [7] N. A. Benedek, A. T. Mulder, and C. J. Fennie, *J. Sol. Stat. Chem.* **195**, 11 (2012).  
 [8] J. T. Heron, J. L. Bosse, Q. He, Y. Gao, M. Trassin, L. Ye, J. D. Clarkson, C. Wang, Jian Liu, S. Salahuddin, D. C. Ralph, D. G. Schlom, J. Íñiguez, B. D. Huey, and R. Ramesh, *Nature* **516**, 370 (2014).  
 [9] S. Fusil, V. García, A. Barthélémy, and M. Bibes, *Annu. Rev. Mater. Res.* **44**, 91 (2014).  
 [10] A. J. Hatt and N. A. Spaldin, *Phys. Rev. B* **82**, 195402 (2010).  
 [11] J. M. Rondinelli and N. A. Spaldin, *Adv. Mater.* **23**, 3363 (2011).  
 [12] J. M. Rondinelli and S. Coh, *Phys. Rev. Lett.* **106**, 235502 (2011).  
 [13] S. J. May, J.-W. Kim, J. M. Rondinelli, E. Karapetrova, N. A. Spaldin, A. Bhattacharya, and P. J. Ryan, *Phys. Rev. B* **82**, 014110 (2010).  
 [14] C. W. Swartz and X. Wu, *Phys. Rev. B* **85**, 054102 (2012).  
 [15] M. Stengel, C. J. Fennie, and Ph. Ghosez, *Phys. Rev. B* **86**, 094112 (2012).  
 [16] J. Hong and D. Vanderbilt, *Phys. Rev. B* **87**, 064104 (2013).  
 [17] M. Dawber, K. M. Rabe, and J. F. Scott, *Rev. Mod. Phys.* **77**, 1083 (2005).  
 [18] K. J. Choi, M. Biegalski, Y. L. Li, A. Sharan, J. Schubert, R. Uecker, P. Reiche, Y. B. Chen, X. Q. Pan, V. Gopalan, L.-Q. Chen, D. G. Schlom, and C. B. Eom, *Science* **306**, 1005 (2004).  
 [19] H. Béa, B. Dupé, S. Fusil, R. Mattana, E. Jacquet, B. Warot-Fonrose, F. Wilhelm, A. Rogalev, S. Petit, V. Cros, A. Anane, F. Petroff, K. Bouzehouane, G. Geneste, B. Dkhil, S. Lisenkov, I. Ponomareva, L. Bellaiche, M. Bibes, and A. Barthélémy, *Phys. Rev. Lett.* **102**, 217603 (2009).  
 [20] M. P. Warusawithana, C. Cen, C. R. Sleasman, J. C. Woicik, Y. Li, L. Fitting Kourkoutis, J. A. Klug, H. Li, P. Ryan, L.-P. Wang, M. Bedzyk, D. A. Muller, L.-Q. Chen, J. Levy, and D. G. Schlom, *Science* **324**, 367 (2009).  
 [21] J. C. Wojdeł and J. Íñiguez, *Phys. Rev. Lett.* **105**, 037208 (2010).  
 [22] C. Lichtensteiger, P. Zubko, M. Stengel, P. Aguado-Puente, J.-M. Triscone, P. Ghosez, and J. Junquera, in *Oxides Ultrathin Films: Science and Technology*, edited by G. Pacchioni and S. Valeri (Wiley-VCH, Germany, 2011), Chap. 12, p. 265.  
 [23] P. Ghosez and J. Junquera, *J. Comp. Theor. Nanosci.* **5**, 2071 (2008).  
 [24] P. Zubko, N. Jecklin, A. Torres-Pardo, P. Aguado-Puente, A. Gloter, C. Lichtensteiger, J. Junquera, O. Stéphan, and J.-M. Triscone, *Nano Lett.* **12**, 2846 (2012).  
 [25] J. Sinsheimer, S. J. Callori, B. Bein, Y. Benkara, J. Daley, J. Coraor, D. Su, P. W. Stephens, and M. Dawber, *Phys. Rev. Lett.* **109**, 167601 (2012).  
 [26] M. Dawber, C. Lichtensteiger, M. Cantoni, M. Veithen, P. Ghosez, K. Johnston, K. M. Rabe, and J.-M. Triscone, *Phys. Rev. Lett.* **95**, 177601 (2005).  
 [27] M. Dawber, N. Stucki, C. Lichtensteiger, S. Gariglio, P. Ghosez, and J.-M. Triscone, *Adv. Mater.* **19**, 4153 (2007).  
 [28] I. Souza, J. Íñiguez, and D. Vanderbilt, *Phys. Rev. Lett.* **89**, 117602 (2002).  
 [29] O. Diéguez and D. Vanderbilt, *Phys. Rev. Lett.* **96**, 056401 (2006).  
 [30] M. Stengel, N. A. Spaldin, and D. Vanderbilt, *Nat. Phys.* **5**, 304 (2009).  
 [31] J. C. Wojdeł, P. Hermet, M. P. Ljungberg, P. Ghosez, and J. Íñiguez, *J. Phys.: Condens. Matter* **25**, 305401 (2013).  
 [32] Y. Yang, W. Ren, M. Stengel, X. H. Yan, and L. Bellaiche, *Phys. Rev. Lett.* **109**, 057602 (2012).  
 [33] O. Diéguez, O. E. González-Vázquez, J. C. Wojdeł, and J. Íñiguez, *Phys. Rev. B* **83**, 094105 (2011).  
 [34] M. Guennou, P. Bouvier, G. S. Chen, B. Dkhil, R. Haumont, G. Garbarino, and J. Kreisel, *Phys. Rev. B* **84**, 174107 (2011).  
 [35] S. Prosandeev, D. Wang, W. Ren, J. Íñiguez, and L. Bellaiche, *Adv. Funct. Mater.* **23**, 234 (2013).  
 [36] D. Rahmedov, D. Wang, J. Íñiguez, and L. Bellaiche, *Phys. Rev. Lett.* **109**, 037207 (2012).  
 [37] C. Cazorla and J. Íñiguez, *Phys. Rev. B* **88**, 214430 (2013).  
 [38] R. J. Zeches, M. D. Rossell, J. X. Zhang, A. J. Hatt, Q. He, C.-H. Yang, A. Kumar, C. H. Wang, A. Melville, C. Adamo, G. Sheng, Y.-H. Chu, J. F. Ihlefeld, R. Erni, C. Ederer, V. Gopalan, L. Q. Chen, D. G. Schlom, N. A. Spaldin, L. W. Martin, and R. Ramesh, *Science* **326**, 977 (2009).  
 [39] Y. Yang, M. Stengel, W. Ren, X. H. Yan, and L. Bellaiche, *Phys. Rev. B* **86**, 144114 (2012).

- [40] C. Cazorla and M. Stengel, *Phys. Rev. B* **90**, 020101(R) (2014).
- [41] We perform bulk calculations, but bearing in mind a thin-film and/or superlattice geometry, where such conditions of strain and electric field can be experimentally achieved.
- [42] I. A. Kornev, S. Lisenkov, R. Haumont, B. Dkhil, and L. Bellaiche, *Phys. Rev. Lett.* **99**, 227602 (2007).
- [43] M. Stengel, D. Vanderbilt, and N. A. Spaldin, *Phys. Rev. B* **80**, 224110 (2009).
- [44] X. Wu, D. Vanderbilt, and D. R. Hamann, *Phys. Rev. B* **72**, 035105 (2005).
- [45] O. Diéguez, S. Tinte, A. Antons, C. Bungaro, J. B. Neaton, K. M. Rabe, and D. Vanderbilt, *Phys. Rev. B* **69**, 212101 (2004).
- [46] J. L. Blok, D. H. A. Blank, G. Rijnders, K. M. Rabe, and D. Vanderbilt, *Phys. Rev. B* **84**, 205413 (2011).
- [47] A. J. Hatt, N. A. Spaldin, and C. Ederer, *Phys. Rev. B* **81**, 054109 (2010).
- [48] R. Haumont, P. Bouvier, A. Pashkin, K. Rabia, S. Frank, B. Dkhil, W. A. Crichton, C. A. Kuntscher, and J. Kreisel, *Phys. Rev. B* **79**, 184110 (2009).
- [49] N. A. Pertsev, A. G. Zembilgotov, and A. K. Tagantsev, *Phys. Rev. Lett.* **80**, 1988 (1998).